Reconstruction of Thermodynamic Cycles in a High-Resolution Simulation of a Hurricane

OLIVIER M. PAULUIS

Courant Institute of Mathematical Sciences, New York University, New York, New York, and Center for Prototype Climate Modeling, New York University Abu Dhabi, Abu Dhabi, United Arab Emirates

FUQING ZHANG

Department of Meteorology, and Center for Advanced Data Assimilation and Predictability Techniques, The Pennsylvania State University, University Park, Pennsylvania

(Manuscript received 12 December 2016, in final form 22 May 2017)

ABSTRACT

The relationship between energy transport and kinetic energy generation in a hurricane is analyzed. The hydrological cycle has a negative impact on the generation of kinetic energy. First, in a precipitating atmosphere, mechanical work must also be expended in order to lift water. Second, the injection of water vapor at low relative humidity and its removal through condensation and precipitation reduces the ability of a thermodynamic cycle to generate work. This reduction can be directly quantified in terms of the change in the Gibbs free energy between the water added and removed.

A newly developed approach—namely, the mean airflow as Lagrangian dynamics approximation— is used to extract thermodynamic cycles from the standard output of a numerical simulation of a hurricane. While convection in the outer rainbands is inefficient at producing kinetic energy, the deepest overturning circulation associated with the rising air within the eyewall is an efficient heat engine that produces about 70% as much kinetic energy as a comparable Carnot cycle. This confirms that thermodynamic processes play a central role in hurricane formation and intensification and that the thermodynamic cycles in a hurricane are characterized by high generation of kinetic energy that differ significantly from those found in atmospheric convection.

1. Introduction

Intense winds in hurricanes and typhoons require a continuous generation of kinetic energy within the storm to balance frictional dissipation. The hurricane circulation transports energy received from the warm ocean to the colder atmosphere. In doing so, it acts as a heat engine that produces the kinetic energy necessary to sustain the storm. The ability to generate kinetic energy can be quantified by an efficiency defined as the fraction of the heat input that is converted into kinetic energy. The efficiency depends on multiple environmental factors, such as the temperature of the energy source and sink, or the relative humidity of the air. In this paper, we will review these factors and show how to assess the efficiency for storms simulated in high-resolution atmospheric models.

The Carnot cycle is probably the best known theoretical model for a heat engine. Its efficiency is the maximum efficiency of any closed thermodynamic cycle and is equal to the ratio of the temperature difference between the heat source and sink to the absolute temperature of the heat source. Hurricanes have at times been compared to a Carnot cycle (Emanuel 1986, 2003; Willoughby 1999) in which the energy source is the warm ocean surface and the energy sink corresponds to the radiative cooling of the troposphere. For a typical ocean temperature of about 300 K and tropopause temperature of 200 K, hurricanes would be able to convert up to one-third of the energy input into kinetic energy.

However, not all heat engines act as Carnot cycles. There is a growing body of evidence that the hydrological cycle leads to a substantial reduction of the generation of kinetic energy by Earth's atmosphere. This occurs for two reasons. First, a substantial fraction of the work done by the atmosphere is used to lift water and is subsequently dissipated as precipitation falls to the ground (Pauluis

Corresponding author: Olivier Pauluis, pauluis@cims.nyu.edu

DOI: 10.1175/JAS-D-16-0353.1

et al. 2000; Pauluis and Dias 2012). Second, the atmosphere acts as a dehumidifier that gains water through evaporation in unsaturated air but loses it as liquid water. This corresponds to a thermodynamic transformation in which the reactant (water vapor) has a lower Gibbs free energy state than the product (liquid water or ice). Such reaction cannot occur spontaneously in an isolated system and reduces the ability of the system to generate mechanical work (Pauluis 2011). Several studies (Pauluis and Held 2002a; Laliberté et al. 2015; Pauluis 2016) have confirmed the negative impacts of the hydrological cycle on the atmospheric heat engine efficiency at both the convective and global scales.

This raises the questions of whether hurricanes can generate kinetic energy at a rate expected from a Carnot cycle, and, if so, of why hurricanes would be less affected by moist processes than other atmospheric motions. To address this issue, we will analyze the thermodynamic behavior of an idealized hurricane simulation. Computing the mechanical output of a thermodynamic cycle is straightforward for idealized cycles. This task is more difficult for highly turbulent flows in which the trajectories of air parcels vary greatly and are not periodic. To address this problem here, we use a new analytical framework, the mean airflow as Lagrangian dynamics approximation (MAFALDA; see Pauluis 2016). Under MAFALDA, one first computes the overturning circulation in isentropic coordinates by sorting rising and descending air parcels in terms of their equivalent potential temperature. This mean circulation is then used to construct a set of thermodynamic cycles with the same mass and heat transport as the total flow. The thermodynamic transformations along these cycles are then analyzed to assess the impacts of moist processes on kinetic energy generation in the hurricane.

Section 2 reviews the impacts of the hydrological cycle on the kinetic energy generation in a generic thermodynamic cycle with condensation and precipitation. It shows that the mechanical output of such a cycle is reduced by a Gibbs penalty term that accounts for the addition and removal of water substance in different thermodynamic states. Section 3 describes the MAFALDA procedure and applies it to a hurricane simulation. Section 4 analyzes the thermodynamic cycles in our simulation to show that the thermodynamic cycle associated with ascent within eyewall can achieve an efficiency comparable to that of a Carnot cycle. Our results are summarized in section 5.

2. Impacts of the hydrological cycle on the atmospheric heat engine

We consider a schematic representation of the overturning circulation in a hurricane as presented in Fig. 1.

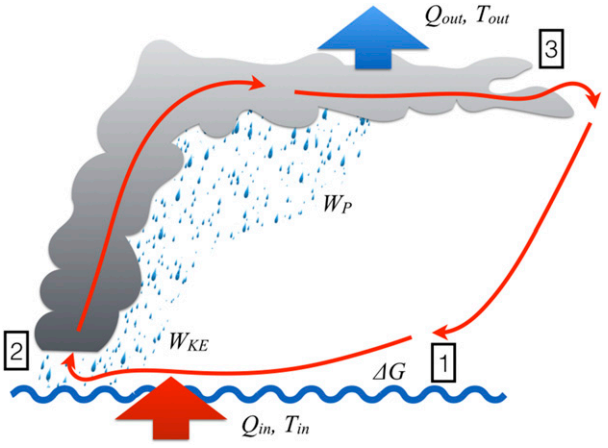

FIG. 1. Schematic representation of a hurricane as a heat engine. Steps 1 → 2: the low-level inflow gains energy from the ocean surface Q_{in}. Steps 2 → 3: air rises from the surface to the upper troposphere, and water condenses and precipitates. Steps 3 → 1: air is gradually compressed back to the surface and loses energy Q_{out} through the emission of infrared radiation. This circulation acts as a heat engine that transports heat from a warm source at temperature T_{in} to a colder sink at temperature T_{out}. This produces mechanical work to generate wind W_{KE} and lift condensed water W_P. The injection of water at the surface and its removal through precipitation are associated with a Gibbs penalty ΔG that reduces the kinetic energy output.

As air rushes toward the center of the storm (points 1 → 2), it gains energy and entropy owing to the energy flux from the surface. It then ascends in the eyewall, undergoing a near-adiabatic expansion, and moves away from the storm center in the upper troposphere (points 2 → 3). The air is eventually brought back to the surface while losing energy through the emission of infrared radiation (points 3 → 1). These transformations correspond to a heat engine that transports energy from the ocean surface to the upper troposphere and is associated with a net conversion of internal energy into kinetic energy.

Quantitatively, we define the efficiency of a heat engine η as the ratio of the generation of kinetic energy W_{KE} to the external heating Q_{in}:

$$\eta = \frac{W_{\text{KE}}}{Q_{\text{in}}}. \tag{1}$$

The potential intensity theory of Emanuel (1986) indicates that a hurricane acts in similar fashion to a Carnot cycle. In particular, the efficiency is equal to the well-known Carnot efficiency η_C:

$$\eta_C = \frac{T_{\text{in}} - T_{\text{out}}}{T_{\text{in}}}, \tag{2}$$

where T_{in} and T_{out} are respectively the temperatures of the energy source and sink.

While the total work and heat flux is proportional to the mass of air being circulated, the efficiency is not. Here, we compute the energy flux and mechanical work per unit mass of dry air circulated. The external heating δq can be directly assessed from the first law of thermodynamics by

$$\delta q = dh - \alpha_d dp. \tag{3}$$

Here, h is the enthalpy per unit mass of dry air, α_d is the specific volume per unit mass of dry air, and p is the total pressure. The external heating here should be understood as external with respect to the parcel. It not only includes energy exchange with the surface and radiative cooling but also diffusive energy transfer and frictional heating. The net energy source Q_{in} and net energy sink Q_{out} are defined as the integral of the positive and negative values of δ_q along the cycle. Integrating Eq. (3) over a cycle yields

$$Q_{\text{in}} + Q_{\text{out}} = W_{\text{KE}} + W_P. \tag{4}$$

The left-hand side here is equal to the net heating, while the right-hand side is equal to the total amount of work produced. The latter is separated into the generation of kinetic energy W_{KE}

$$W_{\text{KE}} = -\oint \alpha_d dp - \oint \Gamma(r_v + r_i + r_l) dz \tag{5}$$

and the work done to lift water

$$W_P = \oint \Gamma(r_v + r_i + r_l) dz. \tag{6}$$

Here, Γ is the gravitational acceleration, and r_v, r_l, and r_i are respectively the mass of water vapor, liquid water, and ice per unit mass of dry air.

To relate the generation of work to the energy transport, we can take advantage of the Gibbs relationship [see Eq. (A.6)] to rewrite the external heating in Eq. (3) as

$$\delta q = Tds + \sum_{w=v,l,i} g_w dr_w. \tag{7}$$

Here, s is the moist entropy per unit mass of dry air, T is the temperature, and g_v, g_l, and g_i are the specific Gibbs free energy for water vapor, liquid water, and ice. The Gibbs free energy terms are necessary here to fully account for the thermodynamic impacts associated with the addition and removal of water in different phases. These quantities are defined in the appendix. Dividing Eq. (7) by the absolute temperature and integrating over a thermodynamic cycle yields

$$\frac{Q_{\text{in}}}{T_{\text{in}}} + \frac{Q_{\text{out}}}{T_{\text{out}}} + \frac{\Delta G}{T_{\text{out}}} = 0. \tag{8}$$

We refer here to the term ΔG as the Gibbs penalty and it is defined as

$$\Delta G = -T_{\text{out}} \oint \sum_{w=v,l,i} \frac{g_w}{T} dr_w. \tag{9}$$

Equations (4) and (8) can be combined to yield an expression for the generation of kinetic energy:

$$W_{\text{KE}} = \frac{T_{\text{in}} - T_{\text{out}}}{T_{\text{in}}} Q_{\text{in}} - W_P - \Delta G. \tag{10}$$

The first term on the right-hand side is the work that would have been produced by a Carnot cycle. The generation of kinetic energy is less than this theoretical maximum because of the work necessary to lift the water W_P and because of the thermodynamic impact of the hydrological cycle quantified in terms of the Gibbs penalty ΔG.

In the idealized cycle, water vapor is added as unsaturated water vapor and removed mostly as liquid water or ice. The Gibbs free energy of unsaturated water vapor is always less than that of liquid water at the same temperature with $g_v - g_l = R_v T \ln \mathcal{H}$, where R_v is the specific gas constant for water vapor and $\mathcal{H}$ is the relative humidity. This implies that water is added to the cycle at a lower Gibbs free energy than it is removed, thus corresponding to a positive value of the Gibbs penalty and a reduction of the mechanical output.

A physical process, such as condensation of unsaturated water vapor, in which the Gibbs free energy of the products is higher than that of the reactants, cannot occur under isothermal and isobaric conditions, as it would imply a violation of the second law of thermodynamics. Indeed, in such a situation, the reverse reaction (e.g., the evaporation of liquid water in unsaturated air) occurs spontaneously. As the transformations involved in the idealized hurricane cycle described in Fig. 1 are neither isothermal nor isobaric, they can result in a net increase in the Gibbs free energy without violating the second law. However, Eq. (10) indicates that, when this happens, the cycle must be associated with a heat transport from warm to cold, and the mechanical output is reduced by an amount equal to the Gibbs penalty.

The difference of Gibbs free energy between water vapor and liquid water, $g_v - g_l = R_v T \ln \mathcal{H}$, is equal to the amount of work that could be produced by the isothermal expansion of water vapor from its saturation partial pressure to its actual partial pressure. And

indeed, this is equal to the amount of work that is produced if water vapor first evaporates in saturated condition then expands to reach the partial pressure in the environment. However, when evaporation occurs in unsaturated air, water molecules irreversibly diffuse into unsaturated air, without generating any mechanical work. Instead, there is an irreversible increase of entropy equal to the increase of Gibbs free energy divided by the absolute temperature. Thus, the Gibbs penalty can be thought of as the amount of work that the thermodynamic cycle fails to produce owing to the thermodynamic irreversibility tied to the hydrological cycle.

3. Reconstruction of thermodynamic cycles from numerical simulations

a. Numerical model and setup

We analyze here the thermodynamic behavior of a hurricane simulated with the Advanced Research version of the Weather Research and Forecasting (WRF-ARW) Model, version 3.1.1 (Skamarock et al. 2008). In this configuration, the model uses three two-way nested domains, with respective sizes of 4320 km by 4320 km, 1440 km by 1440 km, and 720 km by 720 km, and with horizontal grid spacings of 18, 6, and 2 km. The model has 41 vertical levels with the model top at 50 hPa. The two smaller nested domains are moveable, with the domain center following the 850-hPa center of the tropical cyclones. The physical parameterizations are as in Zhang and Tao (2013) and Tao and Zhang (2014). It should be noted that the turbulent parameterization used in WRF does not include a frictional heating—that is, the kinetic energy loss to dissipation is not put back as internal energy. Bister and Emanuel (1998) have suggested that the inclusion of frictional heating can lead to more intense tropical storms. The model is initialized with a modified Rankine vortex with a maximum surface wind speed of 15 m s^{-1} at 135-km radius. The Dunion non–Saharan air layer mean hurricane season sounding (Dunion 2011) is used for the environmental moisture and temperature profile with a constant sea surface temperature of 29°C (SST29) and a constant Coriolis parameter equivalent to 20°N. The initial condition and model setup are as in the noflow-SST29 experiment in Tao and Zhang (2014) but without moisture perturbation.

Figure 2 shows the evolution of the maximum wind and minimum pressure. The hurricane reaches its maximum intensity by the end of day 5, with a central pressure of 885 hPa and a maximum wind speed of 97 m s^{-1}. The storm maintains its intensity for the remaining 10 days of simulation, with a slight increase in surface pressure by day 15. As the experimental setup used here does not include radiative transfer, the atmosphere will slowly evolve toward a state of a thermal equilibrium with the ocean, with no convection or wind. Over the course of the simulation, we observe an increase in low-level humidity away from the storm, a warming of the upper troposphere, and a reduction of the convective activity far away from the storm center. All these are consistent with a slow evolution toward thermal equilibrium. The storm however occupies only a small fraction of the domain and, as noted earlier, its intensity remains steady for the last 10 days of the simulation. Our main focus here is to analyze the thermodynamic cycles that underlie the storm, and we chose here to focus primarily on the intensifying storm on day 5 of the simulation.

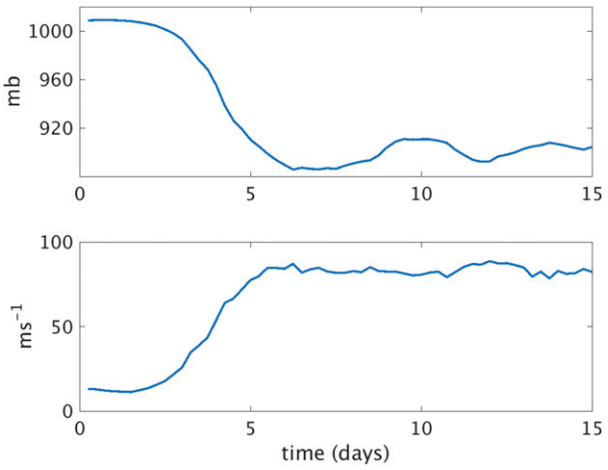

FIG. 2. (top) Minimum pressure and (bottom) maximum tangential wind.

Figure 3a shows the mean azimuthal wind during the fifth day of the simulation. It exhibits a well-defined maximum near the surface at a radius of about 40 km from the storm center. The strong vortex extends through the entire troposphere. Farther away from the center, in the upper troposphere, the circulation is anticyclonic, as evidenced by the negative azimuthal wind.

Figure 3b shows the distribution of equivalent potential temperature θ_e. The equivalent potential temperature here is defined with respect to ice, as in Pauluis (2016). The definition of θ_e used here includes a contribution from the latent heat of freezing and is slightly higher than the equivalent potential temperature over liquid water as defined in Emanuel (1994). Away from the center of the storm, the equivalent potential temperature shows a vertical structure typical of the tropical regions, with high value near the surface, $\theta_e \approx 360$ K, a lower-tropospheric minimum

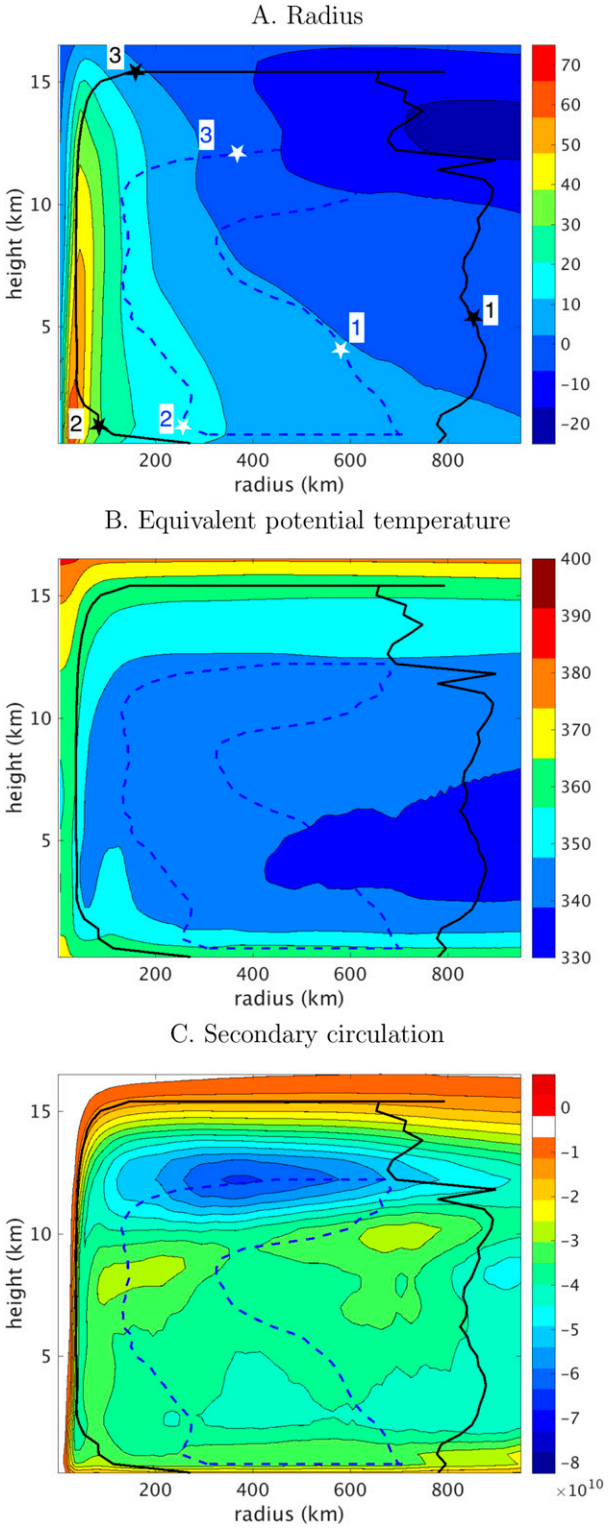

FIG. 3. Time and azimuthal average of the (a) tangential wind, (b) equivalent potential temperature, and (c) streamfunction. The solid black line and the dashed blue line correspond to trajectories associated with the inner-core cycle and rainband cycle, respectively (see section 4). In (a), three locations have been marked along each trajectory: point 1 is the lowest entropy value, point 2 indicates the highest entropy near the surface, and point 3 is the highest point along the cycle.

with $\theta_e \approx 335$ K at an altitude of 4–5 km, then a slow increase in the upper troposphere. The stratosphere is not shown in Fig. 3b but it exhibits an enhanced stratification. Toward the center of the storm, the equivalent potential temperature increases and the midtropospheric minimum of θ_e becomes less pronounced. The eyewall appears as a region of almost constant value of θ_e.

The secondary circulation can be quantified in terms of an Eulerian streamfunction

$$\Psi_E(r,z) = \int_0^r \rho w r dr, \tag{11}$$

which is shown in Fig. 3c. The streamfunction shows a direct overturning circulation, with inflow at low levels, rising motion in the eyewall and outflow in the upper troposphere. Figure 3c also indicates another inflow in the upper troposphere located between 10 and 12 km, below the main outflow. Similar upper-level inflows have been noted in other numerical simulations of hurricanes, such as Rotunno and Emanuel (1987).

b. *The mean airflow as Lagrangian dynamics approximation*

The analysis of the thermodynamic cycles in the previous section requires us to know the evolution of the thermodynamic properties of an air parcel. Most atmospheric flows are highly turbulent, and not only are all parcel trajectories different, but they almost never correspond to a closed thermodynamic cycle. To circumvent this problem, Pauluis (2016) introduced MAFALDA, a systematic approach designed to extract a set of representative cycles from numerical simulations of turbulent atmospheric flows. The method consists of four distinct steps:

(i) compute the isentropic streamfunction in z–θ_e coordinates,
(ii) estimate the conditional average of thermodynamic state variables as function of z and θ_e,
(iii) construct a set of trajectories in z–θ_e coordinates from the isentropic streamfunction, and
(iv) interpolate the values of the various state variables along these trajectories.

1) ISENTROPIC STREAMFUNCTION

Under MAFALDA, one first computes a mean overturning circulation using height z and equivalent potential temperature θ_e as coordinates. It is quantified in terms of the isentropic streamfunction $\Psi(z, \theta_e)$ shown in Fig. 4, defined as the net upward mass flux at height z

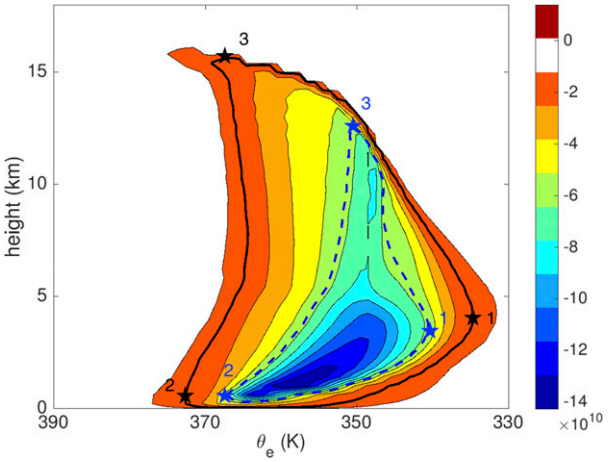

FIG. 4. Isentropic streamfunction in z–θ_e coordinates. The inner-core cycle (solid black line) and the outer cycle (dashed blue line) correspond to two isolines of the streamfunction. Three locations have been marked along each trajectory: point 1 is the lowest entropy value, point 2 indicates the highest entropy near the surface, and point 3 is the highest point along the cycle.

of all air parcels with an equivalent potential temperature less than θ_{e0}:

$$\Psi(z,\theta_{e0}) = \frac{1}{P}\int_{t_0}^{t_0+P}\int_0^{2\pi}\int_0^{r_0}\rho(w-\overline{w}) \times H[\theta_{e0}-\theta_e(r,\phi,z,t)]\,r\,dr\,d\phi\,dt. \quad (12)$$

Here, $P = 1$ day is the time period for the averaging, $r_0 = 800$ km is the radius of the domain used for averaging, ρ is the mass of dry air per unit volume, w is the vertical velocity, $\overline{w}(r, z)$ is the mass-weighted horizontally averaged velocity for $r < r_0$, and H is the Heaviside function. Note that the integral in Eq. (12) is computed only for a central part of the simulated domain. Convection far away for the storm center dominates the isentropic streamfunction when it is computed over the entire domain, making the thermodynamic structure of the hurricane more difficult to distinguish. We choose here to limit the isentropic analysis to an area relatively close to the storm instead. The isentropic streamfunction is introduced in Pauluis and Mrowiec (2013) and its application to hurricanes is discussed in Mrowiec et al. (2016).

The isentropic streamfunction averaged over the fifth day of the simulation is shown in Fig. 4. For a steady flow, the mean flow in z–θ_e coordinates follows the isolines of the streamfunction. In Fig. 4, this flow would be clockwise, with air rising at high value of θ_e near the center of the storm and subsiding at lower θ_e much farther away. The ascent in the eyewall corresponds to rising motions at very high value of θ_e, here for $365 < \theta_e < 380$ K. The ascent of high-θ_e air in the eyewall accounts for only one-third of the total the overturning, with the bulk of the ascent occurring at lower value of θ_e, with $355 < \theta_e < 365$ K.

There are substantial differences between the overturning identified by the Eulerian and isentropic streamfunctions depicted respectively in Figs. 3c and 4. Notably, the mass transport is much larger in the isentropic analysis, with a maximum value of about 1.4×10^{10} kg s^{-1}, than in the Eulerian frame, which has a maximum value of about 0.6×10^{10} kg s^{-1}. The maximum of the isentropic streamfunction is also located near the surface, while the Eulerian streamfunction peaks in the upper troposphere. In addition, the isentropic analysis indicates that rising air parcels exhibit high value of θ_e, with $\theta_e > 355$ K, which is substantially larger than the value of θ_e found in the free troposphere away from the boundary layer and eyewall. These differences can be attributed to the mass transport by convective motions, which is not accounted for by the Eulerian averaging. We will refer the interested readers to Mrowiec et al. (2016) for a more detailed discussion of the difference between isentropic and Eulerian circulations in hurricanes.

2) MAFALDA TRAJECTORIES

In MAFALDA, the isolines of the isentropic streamfunction are treated as parcel trajectories. For a given value of the streamfunction Ψ_0, we construct a parametric representation $[z(\lambda), \theta_e(\lambda)]$ of the isoline such that

$$\Psi[z(\lambda),\theta_e(\lambda)] = \Psi_0. \quad (13)$$

We focus here on two distinct cycles corresponding to 2.5% and 42.5% of the absolute minimum of the streamfunction. Three locations are marked along each cycle: point 1 is the minimum entropy, point 2 corresponds to the maximum entropy at the surface, and point 3 is the highest point in the cycle.

The first trajectory (solid black line) is referred here to as the inner-core cycle and is associated with air parcels rising at very high equivalent potential temperature, with $\theta_e \approx 370$ K. The second trajectory, which we will refer to as the rainband cycle, is representative of air parcels that rise at lower value of the equivalent potential temperature, with $\theta_e \approx 350$ K in the upper troposphere. These two trajectories are shown respectively as the solid black line and the blue dashed lines in Figs. 3a–c. To convert a trajectory in isentropic coordinates θ_e–z, to the Eulerian coordinates r–z, we compute the mean radius associated with air parcels at a given value of z and θ_e as discussed in the next subsection. Figure 3a shows that the inner-core cycle indeed

corresponds to an air parcel that penetrates to near the center of the storm and rises to the tropopause within the eyewall before moving outward and subsiding far away from the center. In contrast, the rainband cycle is associated with rising motion farther away from the center, in the region associated with the outer rainbands of the storms.

3) ISENTROPIC AVERAGE OF STATE VARIABLES

To evaluate the value of the various properties of the air parcels along the streamlines, we compute their mass-weighted conditionally averaged value in z–θ_e coordinates. First, for any function $f(x, y, z, t)$, we introduce its isentropic integral $\langle f \rangle$ as

$$\langle f \rangle(z, \theta_{e0}) = \frac{1}{P} \int_{t_0}^{t_0+P} \int_0^{2\pi} \int_0^{r_0} f \delta[\theta_{e0} - \theta_e(r, \phi, z, t)] r dr \, d\phi \, dt,$$

where δ is the Dirac delta function. The mass-weighted average of f is defined as

$$\tilde{f}(z, \theta_{e0}) = \frac{\langle \rho f \rangle}{\langle \rho \rangle}.$$

Figure 5 shows the isentropic average for the radius $\tilde{r}$, azimuthal wind, specific moist entropy $\tilde{s}$, temperature $\tilde{T}$, mixing ratio $\tilde{r}$, and Gibbs free energy $\tilde{g}_v$, respectively. The radius distribution in Fig. 5a shows that air with high θ_e is preferentially located near the storm center, while low-energy air parcels, with θ_e less than 345 K, are located far away from the center, with $\tilde{r} \geq 500$ km. At low levels, the radius $\tilde{r}$ decreases with increasing θ_e, corresponding to the gradual moistening of the air toward the center of the storm. The azimuthal wind $\tilde{u}$ is shown in Fig. 5b. The strongest wind corresponds to the air with high θ_e near the surface. A benefit of the isentropic averaging here is to magnify the structure of the eyewall. Indeed, while the eyewall occupies a small physical area near the storm center, it is associated with a fairly broad range of high values of θ_e between 355 and 375 K.

Figures 5c and 5d show the distribution of moist entropy $\tilde{s}$ and temperature $\tilde{T}$. There is a close relationship between equivalent potential temperature and entropy, which translates in that the isolines for $\tilde{s}$ are almost vertical. Similarly, the isolines for temperature $\tilde{T}$ are almost horizontal, as the temperature variations are closely tied to changes in height. The water vapor distribution (Fig. 5e) shows high value near the surface and at high equivalent potential temperature. The decreases of water vapor with height are due to the decrease in temperature through the Clausius–Clapeyron relationship. At a given height, fluctuations of water vapor are strongly linked to the horizontal variations of equivalent potential temperature. Figure 5f shows the distribution of the Gibbs free energy of water vapor g_v. The variations of g_v are foremost determined by relative humidity. At high value of θ_e, g_v is close to 0, indicating that these air parcels are saturated with respect to liquid water. Lower values of θ_e are associated with large negative value of g_v in the unsaturated storm environment. In the upper troposphere, the Gibbs free energy is negative as condensation over ice reduces the water vapor pressure well below its saturation value over liquid water.

4) STATE VARIABLES ALONG THE MAFALDA TRAJECTORIES

State variables along given MAFALDA trajectories are taken to be equal to the corresponding isentropic average at the same value of z and θ_e; for example,

$$s(\lambda) = \tilde{s}[z(\lambda), \theta_e(\lambda)].$$

This procedure allows us to estimate the value of any state variable along any of the MAFALDA trajectories. The solid black line and the dashed blue line on Fig. 5 show the MAFALDA trajectories associated with the cycles superimposed on the isentropic average for various state variables.

We apply the MAFALDA procedure to reconstruct the thermodynamic cycles during the fifth day of our simulation. Figure 6 shows the results for the inner-core cycle and the rainband cycles under six different coordinate pairs: moist entropy s and temperature T (Fig. 6a), buoyancy b and height z (Fig. 6b), total water content $r_T = r_v + r_l + r_i$ and height z (Fig. 6c), mixing ratio q and Gibbs free energy for water vapor g_v (Fig. 6d), liquid water content r_l and Gibbs free energy for liquid water g_l (Fig. 6e), and ice water content q_i and Gibbs free energy for ice g_i (Fig. 6f). The axes are chosen so that the trajectories are going clockwise in all four panels, with x and y directions corresponding qualitatively to increasing radius and increasing height. Three locations are marked along each cycles: point 1 is the entropy minimum, point 2 corresponds to the maximum entropy at the surface, and point 3 is the highest point in the cycle.

4. Thermodynamic cycles in a simulated hurricane

The MAFALDA procedure has allowed us to extract thermodynamic cycles from the numerical model output. We now turn to the physical interpretation of the cycles in various thermodynamic coordinates as shown in Fig. 6 and their implications for the generation of kinetic energy.

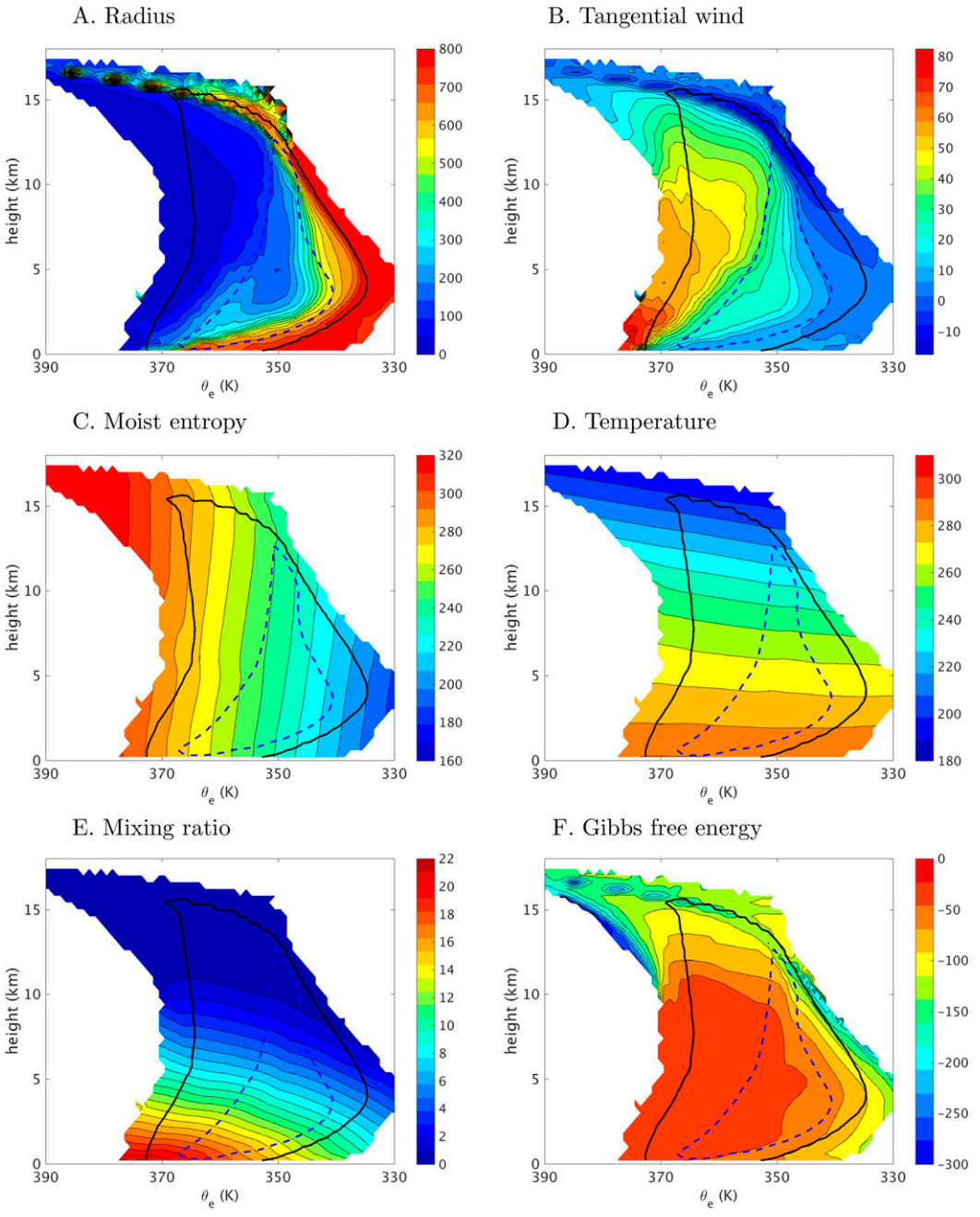

FIG. 5. Isentropic-averaged value for (a) radius, (b) tangential wind, (c) specific moist entropy, (d) temperature, (e) mixing ratio, and (f) Gibbs free energy of water vapor. The solid black line and the dashed blue line correspond to Eulerian trajectories associated with the inner-core cycle and rainband cycle, respectively (see section 4).

In the *T*–*s* diagram (Fig. 6a), the two trajectories exhibit features of a heat engine. For the inner-core cycle, the first transformation from 1 to 2 leads to an entropy increase from 200 to 300 J K^{-1} kg^{-1} due to the energy fluxes from the ocean surface. The second transformation from 2 to 3 corresponds to an expansion with approximately constant moist entropy but decreasing temperature from 300 to about 200 K. In the last leg from 3 to 1, the parcel is compressed back to the surface and its temperature increases from 200 to about 300 K. As first, the parcel loses energy and its entropy decreases from about 300 to 200 J K^{-1} kg^{-1}. Closer to the surface, water vapor gained from mixing with cloudy air leads to an entropy increase from 200 to 240 J K^{-1} kg^{-1}.

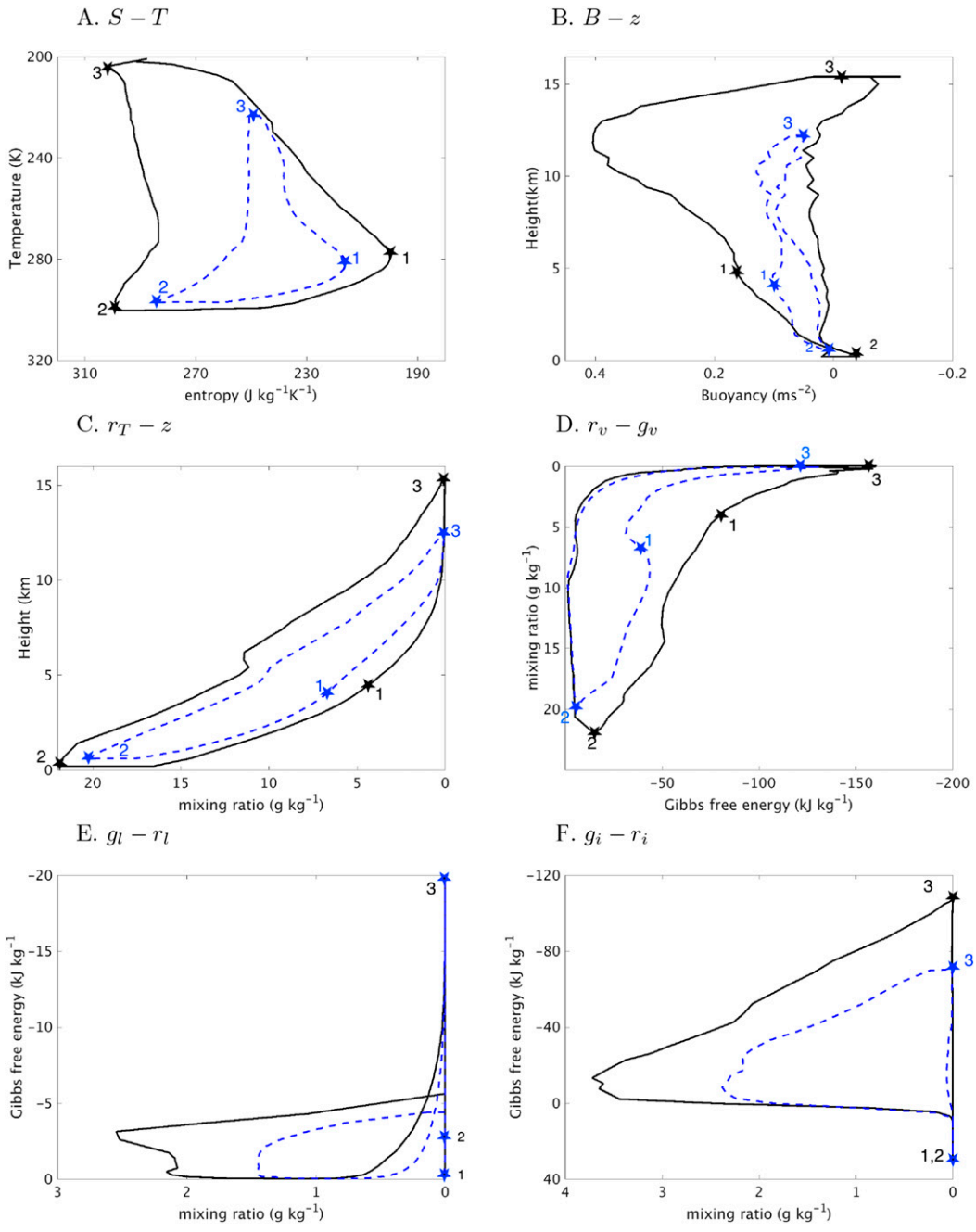

FIG. 6. The inner-core cycle and rainband cycle are shown in different coordinate pairs: (a) specific moist entropy and temperature, (b) buoyancy and height, (c) total water content and height, (d) Gibbs free energy of water vapor and mixing ratio, (e) liquid water content and Gibbs free energy for liquid water, and (f) ice content and Gibbs free energy for ice. The inner-core cycle is shown by the solid black line and the outer cycle by the dashed blue line. The trajectories are clockwise in all panels.

The rainband cycle differs from the inner-core cycle in three aspects. First, the entropy increase in the inflow portion of the cycle ($1 \rightarrow 2$) is substantially less for the rainband cycle indicative of weaker surface energy fluxes. Second, the entropy decreases from about 280 to $250\,\mathrm{J\,K^{-1}\,kg^{-1}}$ during the ascent ($2 \rightarrow 3$). This loss of entropy occurs as the air parcel loses water vapor through detrainment and mixing: a reduction of entropy of $30\,\mathrm{J\,K^{-1}\,kg^{-1}}$ corresponds approximatively to a loss of $3\,\mathrm{g\,kg^{-1}}$ of water vapor. Finally, the rainband cycle is

shallower, reaching a height of 12 km and its minimum temperature (at about 220 K) is substantially warmer than for the inner-core cycle.

Figure 6b shows the two cycles in buoyancy and height coordinates. The buoyancy here is given by

$$b = \Gamma\left[\frac{T-\overline{T}}{\overline{T}} + \frac{R_v}{R_d}(r_v - \overline{r}_v) - (r_T - \overline{r}_T)\right],$$

where the overbar denotes the horizontal average. In an anelastic model, the generation of kinetic energy would be proportional to the integral of $\oint b dz$—that is, the area within the curve shown in Fig. 6b. As the Mach number in a hurricane is high, the anelastic approximation is inaccurate, and the generation of kinetic energy should be computed by the integral (10). Nevertheless, we use here the buoyancy–height coordinates as it makes it easier to visualize the cycles. In both cycles, rising air is lighter than descending air, so that the cycles are associated with a net generation of kinetic energy. The variations of buoyancy in the inner-core cycle are particularly large–reaching up to 0.4 m s^{-2}. The kinetic energy generation is approximately equal to the area within the curve, and Fig. 6b thus indicates that the inner-core cycle generates much more kinetic energy than the rainband cycle.

Figure 6c shows the two cycles in total water mixing ratio and height coordinates. Both cycles corresponds to a net upward transport of water in all phases. The geopotential energy gained by the water as it is lifted by atmospheric motions is proportional to the area within the cycle. The inner-core cycle does more work in order to lift more water to a higher level than the rainband cycle. The maximum mixing ratio in the inner-core cycle is about 22 g kg^{-1}, which is about 2g−kg^{-1} larger than for the outer rainband cycle. This is consistent with the difference of about 20 J K^{-1} kg^{-1} in the maximum entropy between the two cycles and confirms that the entropy increase near the center of the storm is due to the enhanced evaporation from the ocean.

These cycles differ from a Carnot cycle in a more fundamental way: most of the entropy increase arises from the evaporation of water at the ocean surface. The air parcel must be treated as an open system that exchanges water in various phases. Figure 6d shows the two cycles in r_v–g_v coordinates with clockwise trajectories. The Gibbs free energy of water vapor can be approximated as $g_v \approx R_v T \ln \mathcal{H}$ and its variations depend primarily on relative humidity. Surface evaporation 1 → 2 also corresponds to a gain of water vapor at low value of the Gibbs free energy. Expansion 2 → 3 corresponds to a loss of water vapor through condensation and precipitation. As the air is saturated through the expansions, the Gibbs energy of the water vapor closely matches that of liquid water below the freezing level and that of ice above it. During compression 3 → 1, the air parcel gradually gains water vapor from mixing with surrounding clouds. Water is injected into unsaturated air at a low value of the Gibbs free energy (1 → 2 and 3 → 1) but removed during the expansion as condensed water with higher Gibbs free energy (2 → 3). From a thermodynamic point of view, a chemical reaction where the reactant, water vapor, has a lower Gibbs free energy than the product, liquid water, does not occur spontaneously under isothermal conditions. The hydrological cycle is possible here because evaporation occurs systematically at higher temperature than condensation. The difference in Gibbs free energy between evaporation and condensation also leads to a reduction of the kinetic energy generated by the atmospheric heat engine.

Figures 6e and 6f show the two cycles in the mixing ratio and Gibbs free energy for liquid water (g_l–r_l in Fig. 6e) and ice (g_i–r_i in Fig. 6f). These are necessary for the computation of the Gibbs penalty ΔG, but the contribution of the water and ice phase is quite smaller than the contribution from water vapor, owing to the facts that there is much less liquid water and ice present and that the variations of Gibbs free energy for water are small when compared to that of water vapor. The decision here to use liquid water at 273.13 K as the reference state ensures that the Gibbs free energy of water is small and slightly negative.

We apply the thermodynamic framework of section 2 to analyze the kinetic energy generation in each thermodynamic cycle computed from MAFALDA. The energy source Q_{in} and sink Q_{out} are computed by integrating the positive and negative values of the heating increment $\delta q = dh - \alpha_d dp$:

$$Q_{\text{in}} = \oint \max(\delta q, 0) \quad \text{and} \tag{14}$$

$$Q_{\text{out}} = \oint \min(\delta q, 0). \tag{15}$$

The temperature of the energy source T_{in} and sink T_{out} are obtained by

$$\frac{Q_{\text{in}}}{T_{\text{in}}} = \oint \max\left(\frac{\delta q}{T}, 0\right) \quad \text{and} \tag{16}$$

$$\frac{Q_{\text{out}}}{T_{\text{out}}} = \oint \min\left(\frac{\delta q}{T}, 0\right). \tag{17}$$

The Carnot efficiency η_C is equal to the temperature difference between the energy source and energy sink, divided by the temperature of the energy source

$$\eta_C = \frac{T_{\text{in}} - T_{\text{out}}}{T_{\text{in}}}, \tag{18}$$

so that the maximum work that could be achieved by an equivalent Carnot cycle $W_{\max}$ is equal to the product of the net heating multiplied by the Carnot efficiency $W_{\max} = \eta_C Q_{\text{in}}$. The generation of kinetic energy W_{KE} is given by Eq. (5), the work done to lift water W_P by Eq. (6), and the Gibbs penalty by Eq. (9). These quantities are related to each other in terms of the thermodynamic budget (10):

$$W_{\text{KE}} = W_{\max} - W_P - \Delta G.$$

Note that all the values for the energy flux and work—Q_{in}, Q_{out}, $W_{\max}$, W_P, ΔG, and W_{KE}—are expressed in joules per unit mass of dry air.

For the rainband cycle, our analysis yields an external heating $Q_{\text{in}} = 19.9\,\text{kJ g}^{-1}$ occurring at an average temperature $T_{\text{in}} = 294\,\text{K}$, while the cooling temperature is $T_{\text{out}} = 269\,\text{K}$. The Carnot efficiency for this cycle is $\eta_C = 0.08$, which corresponds to a maximum work $W_{\max} = \eta_C Q_{\text{in}} = 1.68\,\text{kJ kg}^{-1}$. The generation of kinetic energy $W_{\text{KE}} = 0.73\text{kJ kg}^{-1}$, which corresponds to a heat engine efficiency $\eta = W_{\text{KE}}/Q_{\text{in}} = 0.04$. This small efficiency is due both to the fact that a substantial portion of the work is used to lift water, with $W_P = 0.42\,\text{kJ kg}^{-1}$, and to counter the Gibbs penalty $\Delta G = 0.48\,\text{kJ kg}^{-1}$ resulting from the hydrological cycle. These numbers are similar to the those obtained for the deepest MAFALDA cycle in moist convection (Pauluis 2016), which confirms that the rainband cycle is in a similar thermodynamic regime as deep convection in the tropics.

In contrast, the inner-core cycle is associated with a larger energy transport, with a net heating of $Q_{\text{in}} = 33.6\,\text{kJ kg}^{-1}$. The temperature of the heat source is marginally lower than for the rainband cycle, with $T_{\text{in}} = 283\,\text{K}$. However, the temperature of the energy sink drops significantly to $T_{\text{out}} = 233\,\text{K}$. As the cycle acts on a larger temperature difference, its Carnot efficiency increases to $\eta_C = 0.18$. This larger Carnot efficiency combined with a larger energy transport leads to a large increase of the maximum work to $W_{\max} = 5.91\,\text{kJ kg}^{-1}$. The negative contributions from water lifting $W_P = 0.87\,\text{kJ kg}^{-1}$ and Gibbs penalty $\Delta G = 0.76\,\text{kJ kg}^{-1}$ increase as well, but not at the same rate as the maximum work. The kinetic energy generation $W_{\text{KE}} = 4.18\,\text{kJ kg}^{-1}$ is less than the theoretical maximum and corresponds to a heat engine efficiency $\eta = 0.13$ for the inner-core cycle.

Our analysis indicates that a striking sixfold increase in kinetic energy generation between the rainband cycle and the inner-core cycle is due to a combination of three changes: 1) a 60% increase in the external heating associated with the intense evaporation at the center of the storm, 2) a substantial decrease in the cooling temperature (from 269 to 233 K) that results in a doubling of the Carnot efficiency, and 3) the actual efficiency of the cycle becomes close to its Carnot efficiency. This later point can be attributed to the fact that relative increases in water lifting W_P and in Gibbs penalty ΔG are much weaker than the relative increase in $W_{\max}$. As a result, while the heat engine efficiency of the rainband cycle was only about 40% of the corresponding Carnot efficiency η_C, the inner-core cycle achieves about 70% of its Carnot efficiency.

The increase in surface heating between the rainband and inner-core cycles is a consequence of the enhanced surface evaporation near the storm center, which has long been recognized as one of the key requirements for the maintenance of hurricane. Enhanced evaporation by itself may not be sufficient however. Indeed, the maximum intensity theory of Emanuel (1986) shows that the maximum wind depends not on entropy itself but on the entropy gradient near the storm center. To be effective, surface evaporation must lead to a local increase in the moist entropy. The ratio $Q_{\text{in}}/T_{\text{in}}$ is the amount of entropy that a parcel gains from the energy source. In our simulation, the high value of Q_{in} for the inner-core cycle is tied to the fact that the air parcels rising within the eyewall have an equivalent potential temperature—about 370 K—that is substantially larger than that of the environment.

The reduction of cooling temperature T_{out} from 269 to 233 K between the rainband and inner-core cycles leads to a substantial increase in the Carnot efficiency. The reduction in cooling temperature can be partially attributed to the deepening of the cycle, as the inner-core cycle reaches a height of 15 km instead of 13 km for the rainband cycle. However, this fact does not by itself explain the large drop in T_{out}. Indeed, a closer look at the s–T diagram for both cycles in Fig. 6a reveals that the lowest temperature in rainband cycle is about 220 K, which is not much different than the minimum temperature in the inner-core cycle—about 200 K. The cooling temperature T_{out} corresponds to the (harmonic) average temperature at which the parcel loses energy. In the rainband cycle, there is a very clear loss of entropy—and energy—during the ascent $2 \rightarrow 3$ owing to the entrainment of dry air in the convective updrafts. This energy loss occurs at warm temperature, between 275 and 300 K, and shifts the cooling temperature toward higher values. In contrast, the ascent in the inner-core cycle is almost adiabatic, and most of the entropy loss occurs during the subsidence at low temperature. Thus, the low cooling temperature and high Carnot efficiency in the

inner-core cycle require not only a deep overturning—so that cooling can occur at low temperature—but also a lack of entrainment during the ascent—which would otherwise correspond to an energy loss at relatively warm temperature.

Finally, the high generation rate of kinetic energy in the inner-core cycle is due in part to the fact that this cycle is able to achieve an efficiency that is close to the Carnot efficiency. While both the Gibbs penalty ΔG and the water loading W_P nearly double between the rainband and the inner-core cycles, the maximum work $W_{\max}$ more than triples. Pauluis (2016) argue that the Gibbs penalty and water loading depends primarily on how much water is added and removed through a thermodynamic cycle and are only weakly sensitive to the depth of the cycle. As such, deep thermodynamic cycles are less hindered by moist processes and their efficiency is closer to their Carnot efficiency.

We further analyze 20 cycles from MAFALDA, ordered from the deepest inner-core cycle 1 to the shallowest cycle 20, with the rainband cycle described above corresponding to cycle 8. The cycles are constructed from different values of the streamfunction and are ordered from the deepest to the shallowest. Figure 7a shows the four terms from Eq. (10). Deep cycles transport more energy across a larger temperature difference and are associated with large value of the maximum work $W_{\max}$. Kinetic energy generation exhibits even a higher sensitivity to cycle depth: it is only a small fraction of the maximum work for shallow cycles but accounts for most of it for the deepest cycle. Both the Gibbs penalty and water lifting also increase with the depth of the cycle, but the sensitivity to the cycle depth is relatively small when compared to either $W_{\max}$ or W_{KE}.

Figure 7b compares the actual efficiency to the Carnot efficiency for each cycle. Deep cycles not only exhibit a higher Carnot efficiency, but they achieve an actual efficiency close to its theoretical maximum. This indicates that, while the hydrological cycle acts to greatly reduce the kinetic energy output of shallow convection, it only marginally reduces the output of deep overturning flows such as the inner-core cycle. Finally, Fig. 7c shows the temperature of the heat source T_{in} and heat sink T_{out}. This confirms that the increase in efficiency is directly related to the deepening of convection and the decrease in the cooling temperature.

Figure 8 shows the evolution of the thermodynamic properties of the deepest MAFALDA cycle through the 15 days of our simulation. This cycle is associated with the value of the isentropic streamfunction equal to 2.5% of its absolute minimum, which corresponds to the inner-core cycle discussed earlier. The four terms of the kinetic energy budget (10) are shown in Fig. 8a. Both

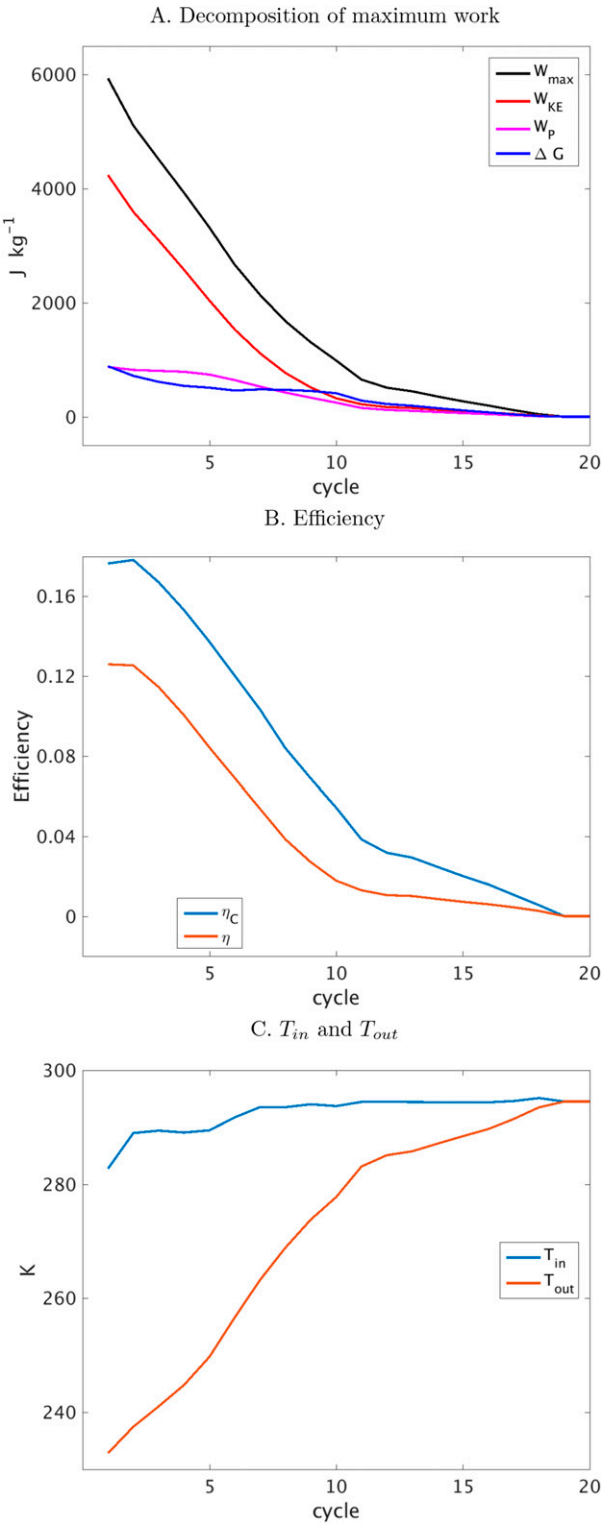

FIG. 7. Thermodynamic analysis for 20 MAFALDA cycles. (a) Decomposition of the maximum work $W_{\max}$ (black) into the generation of kinetic energy W_{KE} (red), water lifting W_P (magenta), and Gibbs penalty ΔG (blue). The inner-core cycle corresponds to cycle 1 and the outer cycle to cycle 8. (b) Comparison between the Carnot efficiency η_C (blue) and the effective efficiency η (red) for each cycle. (c) Temperature of the energy source T_{in} (blue) and energy sink T_{out} (red) for each cycle.

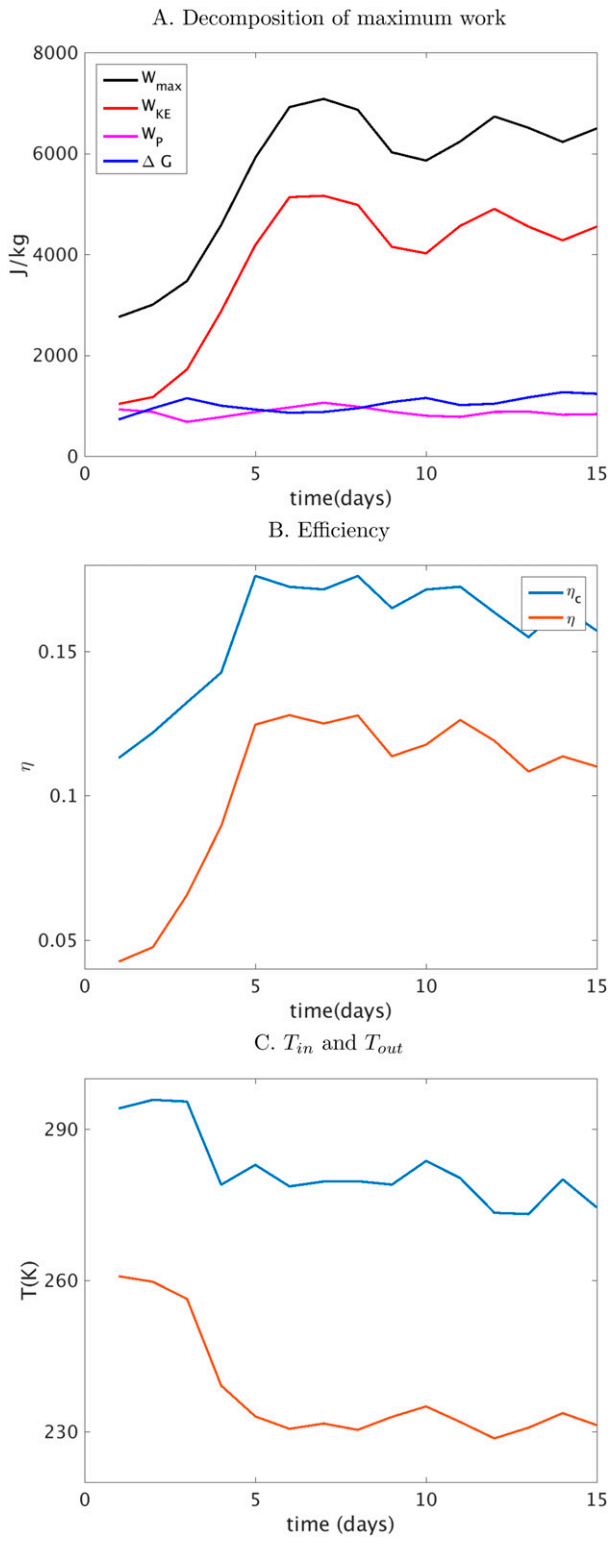

FIG. 8. Time evolution of the MAFALDA cycle associated 2.5th percentile of the isentropic streamfunction, which corresponds to the inner-core cycle discussed in section 4. (a) Decomposition of the maximum work $W_{\max}$ (black) into the generation of kinetic energy W_{KE} (red), water lifting W_P (magenta), and Gibbs penalty ΔG (blue). (b) Comparison between the Carnot efficiency η_C (blue) and effective efficiency η (red). (c) Temperatures of the energy sources T_{in} (blue) and of the energy sink T_{out} (red).

the Gibbs penalty ΔG and water loading terms W_P remain steady. The intensification on day 5 is however marked by a sharp increase in both the maximum work $W_{\max}$ and kinetic energy generation W_{KE}. This intensification is also evident in the Carnot efficiency η_C and the actual efficiency of the cycle shown in Fig. 8b. The increase in Carnot efficiency is itself due to the reduction in the cooling temperature (Fig. 8c). At the beginning of the simulation, the cooling temperature is about 260 K. It drops sharply to 240 K at day 4, and settles to a value between 230 and 235 K for the remainder of the simulation.

5. Conclusions

In this paper, we have applied MAFALDA to analyze the thermodynamic transformations in a high-resolution simulation of a hurricane. This technique relies on identifying the atmospheric overturning by computing a mean circulation in z–θ_e coordinates and extracting a set of thermodynamic cycles that represent the mean overturning flow. This then allows us to diagnose various thermodynamic transformations that occur through each cycle.

We use MAFALDA here to assess the ability of the hurricane to act as a heat engine. Previous studies (Pauluis and Held 2002a,b; Pauluis 2016; Laliberté et al. 2015) have demonstrated that the hydrological cycle has a negative impact on the ability of the atmosphere to generate kinetic energy. This arises from two key aspects of the hydrological cycle. First, mechanical work must be performed in order to lift water and is then lost through frictional dissipation as condensed precipitates (Pauluis et al. 2000). Second, the atmosphere acts partially as a dehumidifier, in which water is introduced as unsaturated water vapor and removed as a condensate. From a thermodynamic point of view, the water has a lower Gibbs free energy when it enters the atmosphere than when it is removed. This results in a reduction of the amount of work that can be produced by the atmospheric circulation (Pauluis 2011). For moist convection, previous studies (Pauluis and Held 2002a; Pauluis 2016) have found that the generation of kinetic energy of moist convection in radiative convective equilibrium is about 10%–20% of the work that could be done by a Carnot cycle acting between the same energy sources and sinks.

Here, we contrast two thermodynamic cycles associated with different trajectories in our simulation: a rainband cycle associated with air ascending in the outer rainband located about 200 km away from the storm and an inner-core cycle corresponding to air rising within the eyewall. These two cycles exhibit very

different thermodynamic behavior, and, in particular, the generation of kinetic energy for the inner-core cycle is approximately 6 times larger than for the rainband cycle. We identify three different factors contributing to the high generation rate of the inner-core cycle: 1) an enhancement of the energy transport by the cycle; 2) a very low cooling temperature, characteristic of the upper troposphere, which results in a very high Carnot efficiency; and 3) a relatively small negative contribution from the hydrological cycle, so that the actual efficiency of the inner-core cycle is about two-thirds of its Carnot efficiency.

The high rate of generation of kinetic energy in the inner-core cycle is strongly tied to the nature of the rising motions within the eyewall. The ascent in the rainband cycle shows a clear indication of entrainment as a gradual decrease of entropy and equivalent potential temperature as the air rises. In contrast, the ascent in the inner-core cycle shows little indication of entrainment of dry air and is almost isentropic. The ascent in the inner-core cycle reaches very high and is associated with very low cooling temperature, which greatly increases the Carnot efficiency. In our simulation, a drop in cooling temperature and a corresponding increase in efficiency precede intensification by about one day. While our work here is limited to a single storm, it strongly suggests that entrainment of dry air into the eyewall, or rather the lack thereof, plays an important role in the intensification and energetics of tropical cyclones.

The methodology of MAFALDA is designed to analyze the thermodynamic processes in a numerical simulation. The physical insights it provides should be tempered by the fact that a numerical simulation is at best a good faith effort at reproducing a physical flow. In particular, the horizontal resolution of 2 km here is too coarse to fully capture the turbulent nature of entrainment. While we strongly believe that the results presented here are both physically consistent and robust, understanding how numerical resolution and the various physical parameterizations affect the behavior of simulated atmospheric flows remains an important challenge in atmospheric science. Assessing thermodynamic processes represented in such numerical simulations should be an essential component of such an endeavor.

The novel approach introduced in this study offers a unique perspective on the role played by thermodynamic processes in hurricane formation and intensity. Our study indicates that the atmospheric circulation in a hurricane, characterized by very high generation of kinetic energy, is in a different thermodynamic regime than tropical deep convection. The genesis and intensification of tropical cyclones correspond to the emergence of deep and highly efficient thermodynamic cycles. Systematic applications of MAFALDA should shed further light on how such cycles emerge, and how energy exchanges with both the ocean surface and the surrounding environment can impact the storm intensity and structure, and on how hurricanes and tropical storms behave under different climates.

Acknowledgments. Olivier Pauluis is supported by the New York University Abu Dhabi Research Institute under Grant G1102. Fuqing Zhang is partially supported by ONR Grant N00014-15-1-2298. The WRF simulation is performed and archived at the Texas Advanced Computing Center. We thank Dandan Tao for running the numerical simulation used in this study. We benefited from discussions with Kerry Emanuel and Juan Fang.

APPENDIX

Gibbs Relationship for Moist Air

The specific Gibbs free energy is defined as the difference between the specific enthalpy and the specific entropy multiplied by the absolute temperature:

$$g = h - Ts.$$

The specific entropy and specific enthalpy depend on the reference state and so does the Gibbs free energy. In this study, we use liquid water at the freezing temperature T_f as the reference state. The specific enthalpies of water vapor h_v, liquid water h_l and ice h_i are

$$h_v = C_l(T - T_f) + L_v, \tag{A1a}$$

$$h_l = C_l(T - T_f), \quad \text{and} \tag{A1b}$$

$$h_i = C_i(T - T_f) + L_{f0}. \tag{A1c}$$

Here, C_l and C_i are the specific heat of liquid water and ice, L_v is the latent heat of vaporization at temperature T, and L_{f0} is the latent heat of fusion taken at the reference temperature T_f. The corresponding specific entropies s_v, s_l, and s_i are

$$s_v = C_l \ln\frac{T}{T_f} + \frac{L_v}{T} - R_v \ln\mathcal{H}, \tag{A2a}$$

$$s_l = C_l \ln\frac{T}{T_f}, \quad \text{and} \tag{A2b}$$

$$s_i = C_i \ln\frac{T}{T_f} - \frac{L_{f0}}{T_f}, \tag{A2c}$$

where R_v is the specific gas constant for water vapor. For this choice of the reference state, the specific Gibbs free energy is therefore

$$g_v = C_l\left(T - T_f - T\ln\frac{T}{T_f}\right) + R_v T\ln\mathcal{H}, \tag{A3a}$$

$$g_l = C_l\left(T - T_f - T\ln\frac{T}{T_f}\right), \quad \text{and} \tag{A3b}$$

$$g_i = C_i\left(T - T_f - T\ln\frac{T}{T_f}\right) - L_{f0}\left(1 - \frac{T}{T_f}\right). \tag{A3c}$$

We treat here moist air as an ideal mixture of 1 kg of dry air, r_v kilograms of water vapor, r_l kilograms of liquid water, and r_i kilograms of ice. The corresponding entropy and enthalpy per unit mass of dry air are

$$s = s_d + r_v s_v + r_l s_l + r_i s_i \quad \text{and} \tag{A4}$$

$$h = h_d + r_v h_v + r_l h_l + r_i h_i. \tag{A5}$$

Here, s_d and h_d are the specific entropy and enthlapy of dry air. The Gibbs relationship relates the change in entropy to changes in enthalpy, pressure, and composition:

$$Tds = dh - \alpha_d dp - \sum_{w=v,l,i} g_w dr_w. \tag{A6}$$

Here, the specific volume α_d is the specific volume per unit mass of dry air:

$$\alpha_d = \frac{R_d T + R_v r_v T}{p}. \tag{A7}$$

REFERENCES

Bister, M., and K. A. Emanuel, 1998: Dissipative heating and hurricane intensity. *Meteor. Atmos. Phys.*, **65**, 233–240, doi:10.1007/BF01030791.

Dunion, J. P., 2011: Rewriting the climatology of the tropical North Atlantic and Caribbean Sea atmosphere. *J. Climate*, **24**, 893–908, doi:10.1175/2010JCLI3496.1.

Emanuel, K. A., 1986: An air-sea interaction theory for tropical cyclones. Part I: Steady maintenance. *J. Atmos. Sci.*, **43**, 585–604, doi:10.1175/1520-0469(1986)043<0585:AASITF>2.0.CO;2.

——, 1994: *Atmospheric Convection.* Oxford University Press, 580 pp.

——, 2003: Tropical cyclones. *Annu. Rev. Earth Planet. Sci.*, **31**, 75–104, doi:10.1146/annurev.earth.31.100901.141259.

Laliberté, F., J. Zika, L. Mudryk, P. J. Kushner, J. Kjellsson, and K. Döös, 2015: Constrained work output of the moist atmospheric heat engine in a warming climate. *Science*, **347**, 540–543, doi:10.1126/science.1257103.

Mrowiec, A. A., O. M. Pauluis, and F. Zhang, 2016: Isentropic analysis of a simulated hurricane. *J. Atmos. Sci.*, **73**, 1857–1870, doi:10.1175/JAS-D-15-0063.1.

Pauluis, O., 2011: Water vapor and mechanical work: A comparison of Carnot and steam cycles. *J. Atmos. Sci.*, **68**, 91–102, doi:10.1175/2010JAS3530.1.

——, 2016: The mean air flow as Lagrangian dynamics approximation and its application to moist convection. *J. Atmos. Sci.*, **73**, 4407–4425, doi:10.1175/JAS-D-15-0284.1.

——, and I. M. Held, 2002a: Entropy budget of an atmosphere in radiative–convective equilibrium. Part I: Maximum work and frictional dissipation. *J. Atmos. Sci.*, **59**, 125–139, doi:10.1175/1520-0469(2002)059<0125:EBOAAI>2.0.CO;2.

——, and ——, 2002b: Entropy budget of an atmosphere in radiative–convective equilibrium. Part II: Latent heat transport and moist processes. *J. Atmos. Sci.*, **59**, 140–149, doi:10.1175/1520-0469(2002)059<0140:EBOAAI>2.0.CO;2.

——, and J. Dias, 2012: Satellite estimates of precipitation-induced dissipation in the atmosphere. *Science*, **335**, 953–956, doi:10.1126/science.1215869.

——, and A. Mrowiec, 2013: Isentropic analysis of convective motions. *J. Atmos. Sci.*, **70**, 3673–3688, doi:10.1175/JAS-D-12-0205.1.

——, V. Balaji, and I. M. Held, 2000: Frictional dissipation in a precipitating atmosphere. *J. Atmos. Sci.*, **57**, 989–994, doi:10.1175/1520-0469(2000)057<0989:FDIAPA>2.0.CO;2.

Rotunno, R., and K. A. Emanuel, 1987: An air–sea interaction theory for tropical cyclones. Part II: Evolutionary study using axisymmetric nonhydrostatic numerical model. *J. Atmos. Sci.*, **44**, 542–561, doi:10.1175/1520-0469(1987)044<0542:AAITFT>2.0.CO;2.

Skamarock, W. C., and Coauthors, 2008: A description of the Advanced Research WRF version 3. NCAR Tech. Note NCAR/TN-475+STR, 113 pp., doi:10.5065/D68S4MVH.

Tao, D., and F. Zhang, 2014: Effect of environmental shear, sea-surface temperature, and ambient moisture on the formation and predictability of tropical cyclones: An ensemble-mean perspective. *J. Adv. Model. Earth Syst.*, **6**, 384–404, doi:10.1002/2014MS000314.

Willoughby, H. E., 1999: Hurricane heat engines. *Nature*, **401**, 649–650, doi:10.1038/44287.

Zhang, F., and D. Tao, 2013: Effects of vertical wind shear on the predictability of tropical cyclones. *J. Atmos. Sci.*, **70**, 975–983, doi:10.1175/JAS-D-12-0133.1.